Univerzita Komenského v Bratislave

Fakulta matematiky, fyziky a informatiky

Alica Brunová

Autoreferát dizertačnej práce

Advanced research of perovskite materials – from bulk to quantum dots

na získanie akademického titulu philosophiae doctor

v odbore doktorandského štúdia:
4.1.4. Kvantová elektronika a optika

Miesto a dátum:
Bratislava, 2022

Dizertačná práca bola vypracovaná v dennej forme doktorandského štúdia

na Fyzikálnom ústave Slovenskej akadémie vied

Predkladateľ: Alica Brunová
Fyzikálny ústav SAV
Dúbravská cesta 9
845 11 Bratislava

Školiteľ: Dr. Rer. Nat. Peter Šiffalovič, DrSc.
Fyzikálny ústav SAV

Odbor: fyzika
Program: 4.1.4. Kvantová elektronika a optika

Predseda odborovej komisie:

Prof. RNDr. Pavel Veis, CSs.
Fakulta matematiky, fyziky a informatiky
Univerzita Komenského
Mlynská dolina F1
842 48 Bratislava

Abstrakt

Perovskitové materiály majú veľký potenciál v optoelektronických aplikáciách. Vlastnosti perovskitov závisia na dimenzionalite, chemickom zložení, štruktúre a celkovej kvalite perovskitu. Všetky tieto parametre ovplyvňujú výkon optoelektronického zariadenia. Úpravou chemického zloženia a spôsobu depozície a žíhania perovskitu môžeme upraviť vlastnosti perovskitu podľa našich potrieb. V tejto práci študujeme niekoľko perovskitových zlúčenín. Ako prvé študujeme vplyv aditíva CH_3NH_3Cl (MACl) v kombinácii s rýchlym žíhaním infračerveným žiarením (FIRA) na kryštalografickú a elektronickú štruktúru a morfológiu dvoj-rozmerného perovskitu $CH_3NH_3PbI_3$ (MAPI). Vrstvy MAPI boli tiež použité na prípravu perovskitových solárnych článkov (PSCs). Ďalej sme skúmali kryštalografickú štruktúru perovskitu $(C_8H_{10}NO_2)_2PbI_4$, v závislosti od substrátu, na ktorom sme tento perovskit deponovali. Nakoniec sme používali perovskitové kvantové bodky $CsPbI_3$ a $CsPbBr_3$ na výrobu fotodetektora.

Abstract

Perovskite materials have been shown to have great potential in optoelectronic applications. Properties of perovskites depend on the dimensionality, chemical composition, structure, and overall quality of the perovskite. All these parameters influence the performance of the optoelectronic device. By chemical engineering, adjustment of deposition, and annealing methods, perovskites can be modified according to our needs. Here we study several perovskite compounds. Firstly, we study the impact of methylammonium chloride (MACl) additive in combination with fast infrared annealing (FIRA) on crystallographic texture, electronic structure, and morphology of methylammonium lead iodide (MAPI) perovskite. MAPI layers were also applied in perovskite solar cells (PSCs). Secondly, we examine the dependence of crystallographic texture of two-dimensional $(C_8H_{10}NO_2)_2PbI_4$ perovskite on the substrate on which the perovskite is deposited. Lastly, we apply $CsPbI_3$ and $CsPbBr_3$ perovskite quantum dots to fabricate photodetector.

Contents

Introduction

Lead halide perovskites (PSKs) have attracted much interest because of their outstanding optoelectronic properties, making them suitable for photovoltaic applications. Only within a decade, power conversion efficiency of solar cells based on three-dimensional (3D) PSKs increased from 3.8% reported by Miyasaka's group to 25.4% reported by M. Kim et al.[1–5]. However, 3D PSKs suffer from poor long-term stability under ambient conditions[6]. To address this issue, two- and zero-dimensional (2D and 0D) PSKs were introduced[7–9]. Reducing the dimensions makes it is possible to improve the optoelectronic properties, especially in 0D PSK[10], which opens the door to applying PSKs in other optoelectronic devices than PSCs, such as LEDs[11] or photodetectors[12].

PSKs can be prepared by low-cost and easy solution processes, which means that there is a potential for scalable industrial fabrication. In laboratories, the PSK layers are traditionally fabricated by spin coating. This technique allows for fast iteration and optimization but is not scalable. A variety of other solution-based deposition methods can be used, such as blade coating, ink-jet printing, etc., setting up a bridge between research and industry. Another improvement in perovskite solar cells (PSCs) fabrication is the annealing by infrared irradiation of PSK layers. This kind of annealing is much faster than conventional hot plate annealing and is easier to use in industrial applications[13].

The optoelectronic properties of PSKs can be adjusted by chemical engineering. In 2D and 3D PSK, it can be done by using additives. Used can be salts, molecules, polymers, or even nanoparticles[14–18]. Additives affect PSK crystal growth. Observed changes are manifested in crystal size, surface morphology, and crystallographic texture of PSK thin films. Moreover, the morphology of 2D and 3D PSKs can be affected by the substrate on which they are deposited[19,20]. Physical properties of 0D PSKs or quantum dots (QDs) depend on the composition, size, and surfactants of PSK QDs[21] and can be adjusted during the synthesis of PSK QDs or by post-synthesis[22,23] and post-deposition[24] treatments. Adapting of PSKs properties is essential to improve PSK device performance.

Here we study several types of PSKs. Firstly, we study 3D methylammonium lead iodide (MAPI) PSK, while methylammonium chloride (MACl) was used as an additive. We are particularly interested in the effects of additive amount on the crystallographic orientation of MAPI PSKs and the formation of the compact layer during annealing by infrared irradiation. Then, the impact of annealing duration on sample surface morphology and trap state density was measured. Furthermore, the MAPI layers were used to fabricate solar cells. Secondly, we

study the growth of 2D PSK with the chemical formula $(C_8H_{10}NO_2)_2PbI_4$ on different substrates: graphene, and fluorine-dopped tin oxide (FTO). We were interested in the morphology and crystallographic orientation of the layers. Lastly, we examine methods of $CsPbI_3$ and $CsPbBr_3$ PSK QDs deposition and post-deposition treatments of the layers. to fabricate a photodetector. QDs layers were also used to fabricate a photodetector.

1 Perovskite materials

The PSKs belong to the family of chemical compounds with the general formula ABX_3, where A and B are cations and X is an anion[25]. Ideally, PSKs crystallize in cubic symmetry. B cation is located in the cube center and is surrounded by six X anions placed in cube faces. Cations are placed in the corners of cube[26]. Formability of PSK structure is given by tolerance factor

$$t = \frac{R_A + R_B}{\sqrt{2}(R_B + R_X)} \tag{1.1}$$

where R_A, R_B, and R_X are the effective radii of A, B, and X ions, respectively[27]. The structure is stable if the value of t is close to 1. When $t = 1$, a cubic structure is expected. For $t < 1$, structural symmetry decreases and may convert to orthorhombic or tetrahedral[28,29]. Fig. 1 shows the PSK structure. In lead halide PSKs, 'A' is a cesium cation or small organic cations (methylammonium or formamidinium). 'B' is occupied by Pb^{2+} cations and on the 'X' side are halogen anions Cl^-, I^-, and Br^-.

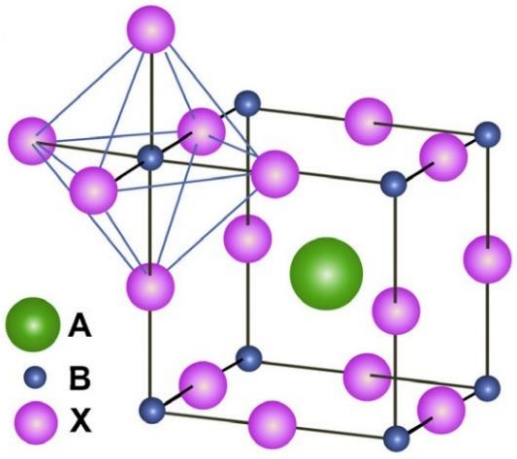

Fig. 1 Structure of perovskite[29].

Recently, research has focused on lead halide PSKs because of their unique electronic structure that combines effective optical absorption, defect tolerance, and low charge carriers recombination[26,30], which determine their charge carrier diffusion length, and effective light emission[31,32]. Due to these physical properties, PSKs can be applied in numerous optoelectronic devices such as solar cells, LEDs, or photodetectors. Additionally, PSK films can be fabricated by low-temperature solution processing methods[33,34]

The peculiarity of PSK materials lies in their modifiability. By tuning the chemical composition of PSKs, we can adjust their physical properties. Moreover, we can easily obtain various nanostructures, ranging from three-dimensional (3D) single crystals and layers, two-dimensional (2D) layered PSKs and nanosheets, one-dimensional (1D) nanorods to zero-dimensional (0D) quantum dots (QDs)[35,36].

1 *Aim of the work*

This work focus on fabrication and characterization of PSK layers suitable for optoelectronic applications, mainly in solar cells. We will study three types of PSK: 3D $CH_3NH_3PbI_3$ (MAPI) PSK, 2D $(CH_{10}NO_2)_2PbI_4$ PSK, and $CsPbI_3$ and $CsPbBr_3$ PSK QDs.

Firstly, we will modify the preparation of the 3D PSK layer by chemical engineering and a novel annealing method. Layers will be characterized by several techniques, namely AFM, GIWASX, and ER-EIS, to study topography, morphology, and electrical properties of 3D PSK layers. We will also study the time development of the 3D PSK layer during the deposition by real-time *in-situ* GIWAXS to correlate the 3D PSK structure with its other properties to determine the ideal processing method. After that, 3D PSK layers will be employed for solar cells fabrication.

Secondly, we will grow 2D PSK layers on different substrates to investigate changes in layer structure depending on the substrate. The structure of layers will be examined by utilizing real-time *in-situ* GIWAXS measurements.

Finally, we will perform pilot experiments with PSK QDs. We will explore several methods of PSK QDs layer fabrication and attempt to use them to fabricate a photodetector.

2 *Experimental techniques*

We employed drop casting, spin coating, and blade coating to deposit PSK layers. The simplest film deposition method is drop casting. The precursor solution is dropped on a substrate and solvent is dried, resulting in solid film formation. When spin coating is used, the precursor solution is dropped onto the substrate, which is then spun at high speed. Because of centrifugal forces, the applied solution spreads all over the sample while the excess liquid is expelled. The sample is annealed to remove all solvent. When blade coating is used to fabricate the PSK layers, the solution is pre-dispersed on the substrate and then spread by the blade moving above the sample. The obtained liquid thin film dries, and a solid film is formed.

Surface topography was measured by AFM and SEM. AFM evaluates the forces between vibrating probe and sample surface. The measured data are processed by imagining software. SEM uses a beam of accelerated electrons to inspect the sample. Electrons scattered by a sample are detected to create an image of the sample surface.

GIWAXS was used to study morphology of PSK films. GIWAXS patterns were measured by table-top custom-designed laboratory system and synchrotron radiation at P03 beamline at PETRAIII facility in DESY (Hamburg, Germany). Both used GIWAXS set-ups are depicted in Fig. 2. In the laboratory, the X-ray beam energy was 8.04 keV (Cu Kα radiation),

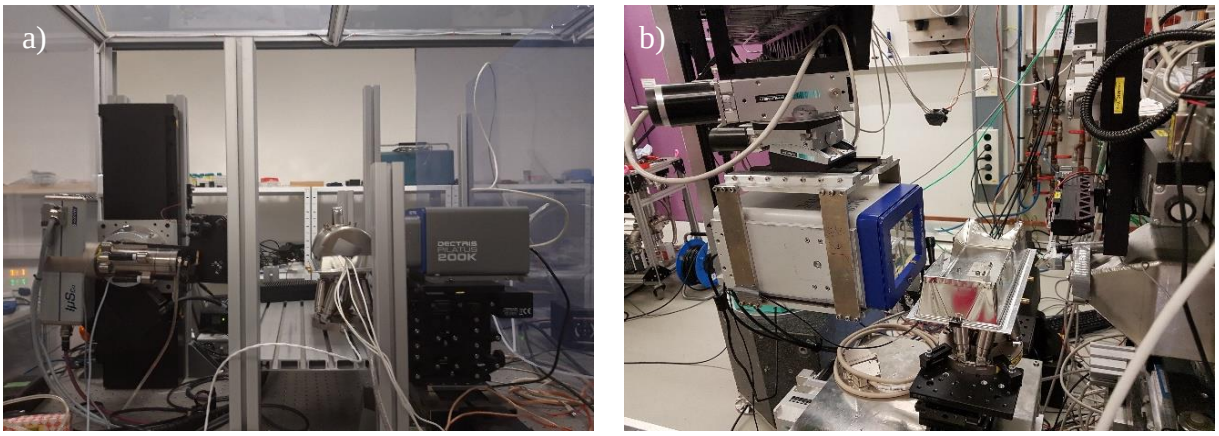

Fig. 2 GIWAXS setup a) in the laboratory, b) at the P03 beamline, PETRAIII, DESY.

corresponding to the wavelength of 1.54 Å. The incidence angle of the X-ray beam on the sample was set to 1.8°. The GIWAXS patterns were registered by a two-dimensional X-ray detector (Pilatus 200K, Dectris). The sample was positioned in a FIRA chamber mounted between the X-ray source and detector. The exposure time in time-resolved measurements of the PSK crystallization was set to 100 ms and the delay interval between the two successive

images was 110 ms. The solution was spin coated on the substrate and the as-prepared sample was inserted into the FIRA chamber. Before starting FIRA, extra 300 images (33 s) were collected. Then FIRA was turned on automatically by sending a signal from the X-ray detector and the sample was annealed for 7.7 s (70 images). After FIRA was turned off, another 1230 images were collected (135.3 s). The total time of measurement was 176 s (1600 images). At the P03 beamline at PETRAIII, the energy of the X-ray was set to 11.4 keV (λ = 1.09 Å). The incidence angle was set to 0.5°. The FIRA chamber was located between the X-ray source and the detector. The GIWAXS patterns were collected by 2D detector (Pilatus 300K, Dectris). The exposure time was 20 ms and the time between the consecutive images was 25 ms. The measurement itself lasted for 50 s (2000 images). Before annealing, the pristine state of the layer was recorded for 10 s. Afterward, a TTL electronic signal from the X-ray detector triggered FIRA to switch on for 10 s. In the post-annealing period, the data were recorded for another 30 s.

The ER-EIS maps the electronic density of states (DOS) between HOMO and LUMO bands in semiconductors. During the measurement, the PSK layer interacts with the electrolyte via an oxidation-reduction reaction in an electrochemical cell. The DOS function *g(E)* in the semiconductor can be directly derived from charge transfer resistance of PSK-electrolyte interface, which is experimentally obtained as a real part of impedance using the superimposed perturbation at a suitable frequency under applied voltage.

The fabricated solar cells are characterized by measuring *JV* curves. The device is illuminated by light with a defined spectrum, which simulates sun radiation. The following solar cell parameters are calculated – short-circuit current density (J_{sc}), open-circuit voltage (V_{oc}), fill factor (*FF*), and power conversion efficiency (*PCE*).

3 Results

3.1 Structural and trap state density enhancement in flash infrared annealed perovskite layers

The following study is focused on the interrealtion between the crystallographic structure and trap state density of MAPI PSK layers with different amounts of MACl additive processed by FIRA. for standard PSK solution PbI_2 and MAI in 1:1 molar ratio were dissolved in DMF and DMSO mixed solvent. When solutions with additives were prepared, the molar

amount of MAI was partially replaced by MACl – 5, 10, 20, 30, 40, and 50%. Then, the selected PSK solution was spin coated on ITO/PEDOT:PSS substrate and annealed by FIRA.

Firstly, we focused on the correlation between the amount of MACl in PSK solution and crystallographic texture of PSK thin film. Fig. 3 shows GIWAXS patterns of the final state of the perovskite layer with 0% MACl and 10% MACl. Without additive, we observed a continuous diffraction ring corresponding to 110/002 diffractions which indicates a random orientation of the perovskite crystals. For 10% of MACl additive, the GIWAXS pattern shows a uniaxial texture with (112) crystallographic planes parallel to the surface of the substrate. When the amount of MACl is more than 10%, 110/002 diffraction spots blur, which suggests an increasing disorder.

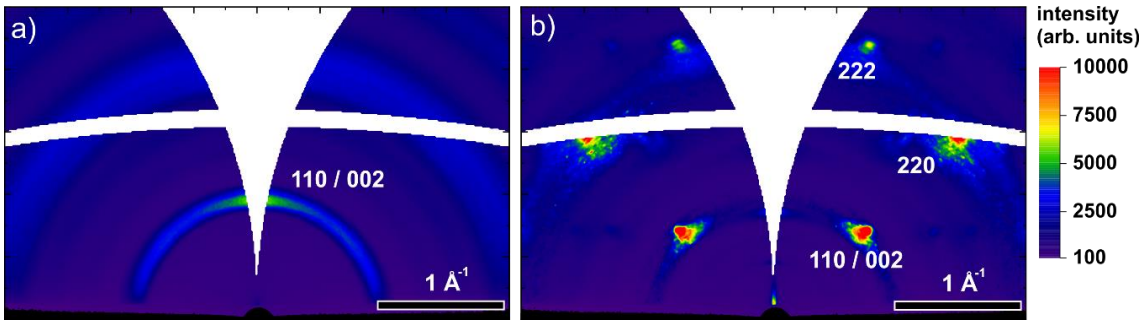

Fig. 3 GIWAXS patterns of perovskite final states for a) 0% MACl, b) 10% MACl.

Based on the observation that 10% of MACl additive gives a highly oriented PSK structure, we fabricated a series of PSK samples with FIRA annealing time ranging from 0.5 s to 10 s. The PSK surface topography was measured by AFM and visible microscopy. The PSK layer was still wet after an annealing for less than 3 s and a needle-like structure was formed during drying. After 3 s of annealing (**Chyba! Nenašiel sa žiaden zdroj odkazov.**b), AFM revealed the presence of needle-like clusters which grow radially from the nucleation centers. However, crystallization was not yet finished. A continuous layer was obtained by annealing for 4 s. The PSK layer consisted of tightly connected clusters several tens of micrometer large.

The trap state density was qualified by the ER-EIS technique. PSK layers were made from a solution with 10% of MACl and annealed for 3, 4, 5, and 6 s by FIRA. The DOS spectra also indicate decreasing trap state density with increasing annealing time. According to these results, the formation of a continuous PSK layer composed from uniaxially oriented crystals leads to a decrease of trap state density in the band gap. We fabricated a PSK layer without MACl additive using the antisolvent method and measured its DOS spectrum to validate this statement. Random orientation of grains of the PSK film prepared by the antisolvent method

was verified by GIWAXS. We compared the DOS of the PSK layer made by the antisolvent method to one annealed by FIRA for 6 s containing 10% of MACl. FIRA processed film had about one order of magnitude lower trap state density than layer fabricated by the antisolvent method. Assuming that low trap state density reduces electron-hole recombination in PSCs, this result implies significant increase of the short-circuit current density of PSCs fabricated by FIRA.

During FIRA, the kinetics of crystal formation was studied by real-time GIWAXS measurements performed for samples with 10% of MACl. During FIRA, we observed the direct formation of uniaxially textured structure. We tracked intensities of PSK peak, precursor diffraction and back-conversion of PSK to PbI_2 during FIRA. We correlated PSK conversion data with trap state density and surface topography. Data are showed in Fig. 4.

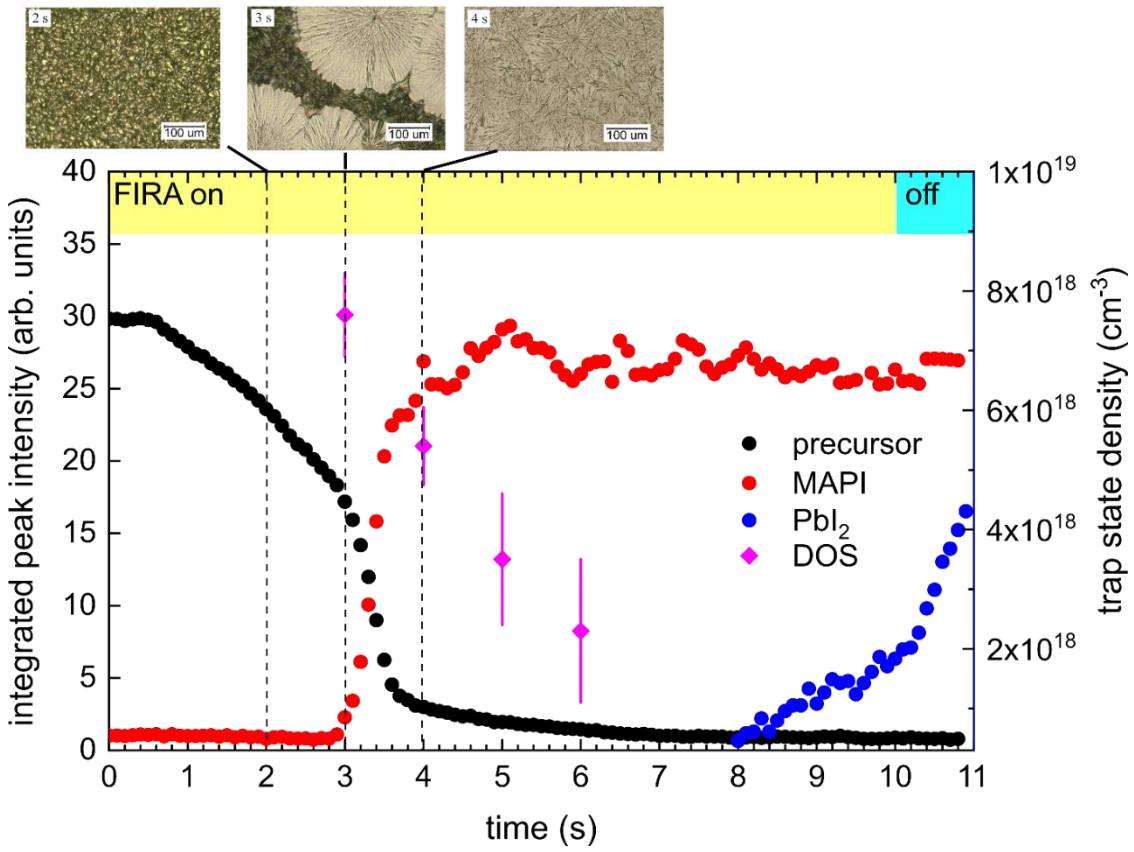

Fig. 4 PSK conversion correlated with trap state density and surface topography.

FIRA started at 0 s and lasted for 10 s. Then FIRA chamber cooled down to room temperature. For the first three seconds, we measured only the precursor signal because the film was still wet. The microscopic image confirmed that the layer crystalized after removing the sample from the FIRA chamber. In the period of 3 - 4 s, we observed rapid crystallization. We also followed it visually as a color change of the film from yellow to black directly in the FIRA

chamber. Samples removed from FIRA after 3 s at the beginning of crystallization were still partially wet. However, microscopic images showed some well-developed crystalline areas. The measured trap state density was around $8x10^{18}$ cm^{-3}. After 4 s of annealing, microscopic images showed continuous PSK film, and trap state density dropped to around $6x10^{18}$ cm^{-3}. According to GIWAXS measurement, conversion of PSK film was not yet completed but continued at a much slower rate. Trap state density decreased proportionally with increasing FIRA time to the value of approximately $2.5x10^{18}$ cm^{-3} for 6 s of FIRA. At 8 s of FIRA processing time, the PSK phase started to convert back to the PbI_2 precursor. This conversion also continued after switching the FIRA off, as conditions remained favorable. In the time-resolved study, we identified a narrow processing window from 6 to 8 s, where prepared PSK films exhibited the lowest traps state density and highest crystallinity.

To test the usability of FIRA processed PSK layers in photovoltaic devices, we fabricated inverted and direct solar cells with architecture standardly used in our laboratories. Composition of inverted PSC was ITO/PEDOT:PSS/PSK/PCBM/BCP/Ag and direct PSC FTO/SnO_2/PSK/ Spiro-OMeTAD/Ag.

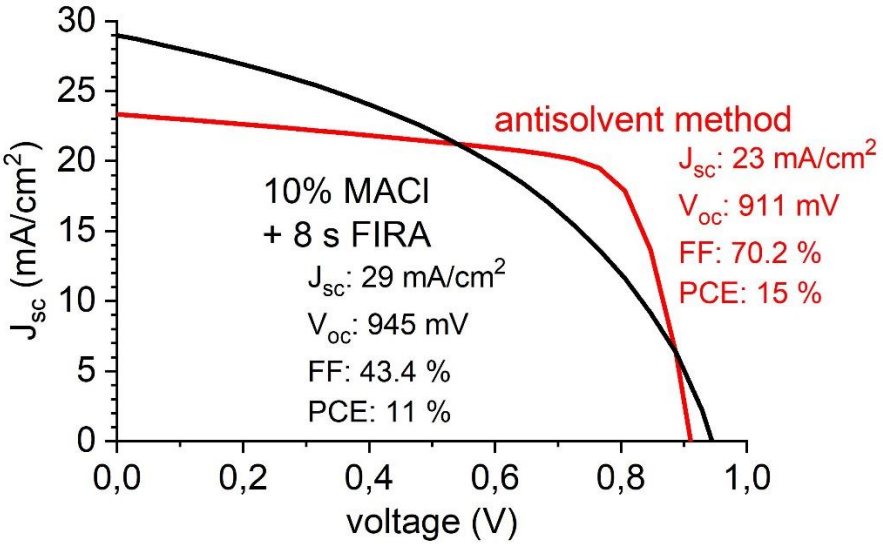

Fig. 5 JV curves of solar cells with PSK layer fabricated from solution with 10% of MACl annealed by FIRA for 8 s and PSK layer made by the antisolvent method with corresponding parameters.

JV curves of inverted PSCs with the corresponding performance parameters are depicted in Fig. 5. The FIRA-annealed device exhibits a higher J_{sc} and V_{oc} value than the standard device using the antisolvent method. This result is in agreement with ER-EIS measurement. Due to the low trap state density in the FIRA processed PSK layer, there is also a lower non-radiative recombination rate. Therefore, values J_{sc} and V_{oc} are higher than those for antisolvent processed

PSC. However, the *FF* of FIRA processed PSC is much lower, which causes a low *PCE*. Low *FF* is usually caused by insufficient quality of layers interfaces. Since the PCBM layer is only 90 nm thick, the rough PSK surface was probably not fully covered. Another problem can be the high temperature in the FIRA chamber, which can partially deteriorate the organic PEDOT:PSS layer. Fabrication of direct PSCs was not successful. We were able to measure only the linear *IV* curve, meaning we did not create a diode structure. There were probably defects in the layers that caused leakage current. More research needs to be done to produce effective PSCs.

3.2 Crystallization of 2D hybrid organic-inorganic perovskite templated by conductive substrates

With this study, we investigated the crystallization of 2D PSK with the chemical formula $(C_8H_{10}NO_2)_2PbI_4$ on conductive substrates, FTO and graphene by utilizing the GIWAXS method. GIWAXS measurements were performed using synchrotron radiation.

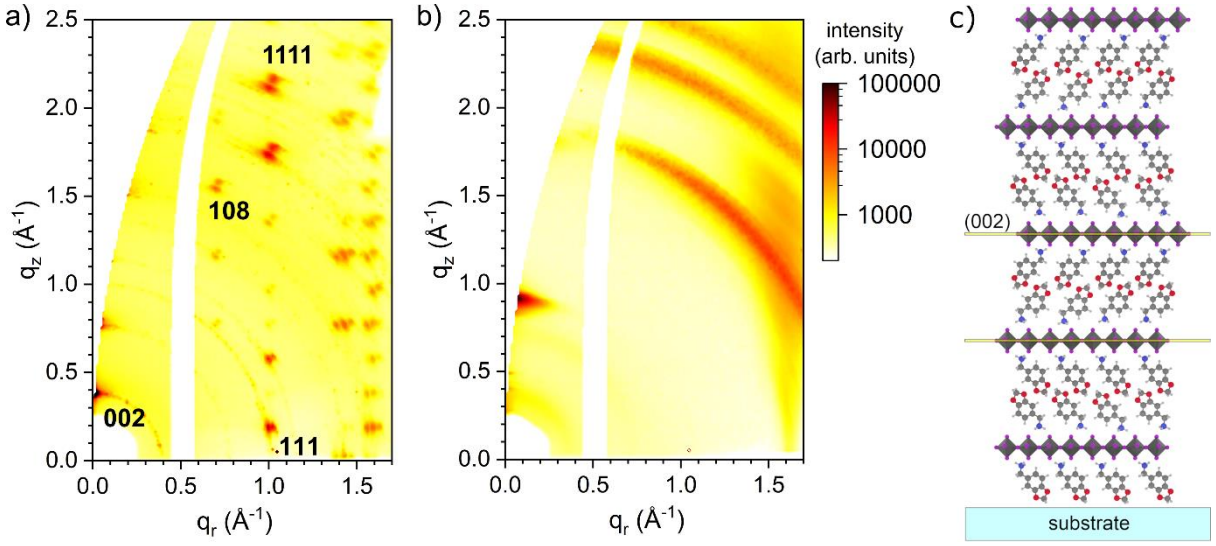

Fig. 6 GIWAXS patterns of 2D PSK layers deposited on a) graphene and b) FTO substrate. c) Schematic structure of 2D PSK layer with (002) planes parallel to the substrate.

Firstly, we studied the impact of a substrate on the orientation of 2D PSK using GIWAXS. GIWAXS patterns of the final state of 2D PSK layers deposited on graphene and FTO substrates are shown in Fig. 6a,b. The 2D PSK film grown on graphene was uniaxially textured with (001) planes parallel to the substrate surface. Diffraction spots were indexed using an orthorhombic crystal system. Please note that the *l*-index is 11 in 1111 diffraction. The higher

diffraction orders occurring in GIWAXS patterns proof layered structure consisting of PbI_6 octahedrons sheets and the organic cations. The schematic structure of such 2D PSK layer with (002) planes parallel to the substrate is depicted in Fig. 6c. The parallel alignment of the (002) planes to the graphene substrate is emphasized. However, 2D PSK film grown on FTO displays 001 diffraction peak at $q \sim 0.9$ Å^{-1} characteristic of PbI_2.

Utilizing real-time GIWAXS measurements, we verified direct growth of highly textured layers on graphene. Our findings show that the 2D PSK crystallization differs depending on the substrate we used. Graphene templated crystallographic texture of 2D PSK, while FTO induced isotropic crystallization.

3.3 Quantum dots

In our experiments, we used commercially available PSK QDs with the chemical formulas $CsPbI_3$ (Quantum Solutions) and $CsPbBr_3$ (Sigma Algrich) capped in oleylamine and oleic acid mixed surfactants. $CsPbI_3$ QDs were dispersed in octane and $CsPbBr_3$ QDs were dispersed in toluene. Original PSK QDs solutions concentration was 10 mg/ml. Solutions were modified to obtain concentrations of 30, 40, 50 and, 60 mg/ml. PSK QDs were deposited on two kinds of substrates, Si/SiO_2 and ITO/PEDOT:PSS.

We fabricated PSK QDs photodetector using the same procedure as for inverted PSCs. Instead of the MAPI PSK layer, we deposited the PSK QDs layer. PSK QDs layers were deposited by various techniques thickness – spin coating, blade coating, and drop casting – that affect the and surface roughness of the layer. However, we were unable to quantify them by AFM because of layer degradation during measurement. Photodetectors were characterized by *JV* curve measurements. For most photodetectors with PSK QDs layer deposited by spin coating and blade coating, we obtained a linear *JV* curve. PSK QDs layers were probably too thin and not continuous, resulting in current leakage. The rest of the devices were not electrically conductive. PSK QDs layer probably acted as an insulator.

To fabricate a conductive $CsPbI_3$ PSK QDs layer, we attempted to perform a so-called solid-state ligand exchange[9,24,37]. This method consists of washing the PSK QDs layer with ligand exchange solutions (LES), during which long-chain oleylamine and oleic acid are substituted by a shorter acetyl moiety. Firstly, the PSK QDs layer is deposited. LES solution is spin coated on the PSK QDs layer or the sample is dipped into the LES solution. Then, the sample is washed with methyl acetate. As an LES, we used saturated sodium acetate, lead acetate, and lead nitride solutions in methyl acetate. Unfortunately, we were not able to fabricate

a PSK QDs layer suitable for further applications by this procedure, because during the washing procedure, a significant part of the PSK QDs layer was removed from the sample.

Conclusion

We studied various PSK materials with the aim of their application in optoelectronic devices. All PSK layers were fabricated by solution processing, as it is a simple and inexpensive way of PSK layer production.

Firstly, we examined the impact of the MACl additive contained in PSK precursors solution in combination with FIRA annealing on MAPI PSK structure. By utilizing GIWAXS measurements, we found that the ideal molar amount of MAI substituted by MACl is 10%. With this substitution, we obtained highly textured MAPI films with (112) crystallographic planes parallel to the substrate surface. According to ER-EIS, FIRA processed MAPI layers with 10% of MACl had approximately one magnitude lower trap state density than MAPI layers prepared by a conventional antisolvent method that exhibited random crystallographic orientation. Utilizing real-time GIWAXS measurements during FIRA annealing and correlating these measurements with ER-EIS and surface topography measurements, we identified an optimal processing window from 6 to 8 s of FIRA. MAPI PSK layers annealed for 8 s were used to fabricate PSCs. The inverted solar cell exhibited higher J_{sc} and V_{oc} in comparison with the reference prepared by the antisolvent method. However, values of *FF* and *PCE* were low, probably because of the insufficient quality of solar cell layers interfaces. Fabrication of direct PSC was not successful, and the devices were not working. By our experiments, we showed a way of improvement of the MAPI PSK layers and the possibility of fast and scalable fabrication that could be eventually applied in industrial manufacturing. However, PSCs fabrication needs further research to be able to manufacture effectively working devices.

Similarly to 3D PSKs, the performance of optoelectronic devices based on 2D PSK depends on the structure and texture of the 2D PSK film. Therefore, we studied the growth of 2D PSK with the chemical formula $(C_8H_{10}NO_2)_2PbI_4$ two kinds of substrates: graphene and FTO coated glass. Again, PSK films were annealed by FIRA because of their duration and scalability. On FTO, we observed isotropic crystallization while 2D PSK layers grown on graphene were highly textured. Our findings show the importance of the choice of the substrate to obtain desired 2D PSK film properties for the selected optoelectronic device.

Finally, we performed several experiments with $CsPbI_3$ and $CsPbBr_3$ PSK QDs with the aim of photodetector fabrication. The architecture of the photodetector was the same as the architecture of inverted PSC. QDs were deposited utilizing three different methods: spin coating, blade coating, and drop casting. However, any device was not working due to a lack of PSK QDs conductivity. Therefore, we attempted to perform a so-called solid-state ligand exchange to improve the conductivity of PSK QDs. Unfortunately, we were not successful.

Scientific outputs

Publications:

Brunova, **Alica;** Vegso, Karol; Nadazdy, Vojtech; Nadazdy, Peter; Subair, Riyas; Jergel, Matej; Majkova, Eva; Pandit, Pallavi; Roth, Stephan V.; Hinderhofer, Alexander; Schreiber, Frank; Tian, Jianjun and Siffalovic, Peter: *Structural and Trap-State Density Enhancement in Flash Infrared Annealed Perovskite Layers.* Advanced Material Interfaces 2021, DOI: 10.1002/admi.202100355

Kovaricek, Petr; Nadazdy, Peter; Pluharova, Eva; **Brunova**, **Alica**; Subair, Riyas ; Vegso, Karol; Guerra, Valentino L. P.; Volochanskyi, Oleksandr; Kalbac, Martin; Krasnansky, Alexander; Pandit, Pallavi; Roth, Stephan V.; Hinderhofer, Alexander; Majkova, Eva; Jergel, Matej; Tian, Jianjun; Schreiber, Frank; and Siffalovic, Peter: *Crystallization of 2D Hybrid Organic–Inorganic Perovskites Templated by Conductive Substrates*. Advanced Functional Materials 2021, DOI: 10.1002/adfm.202009007

Bodik, Michal; Demydenko, Maksym; Shabelnyk, Tetiana; Halahovets, Yuriy; Kotlar, Mario; Kostiuk, Dmytro; Shaji, Ashin; **Brunova, Alica**; Veis, Pavel; Jergel, Matej; Majkova, Eva; Siffalovic, Peter: *The Collapse Mechanism in Few-Layer MoS2 Langmuir Films*. The Journal of Physical Chemistry C 124(29). 2020, DOI: 10.1021/acs.jpcc.0c02365

Posters at conferences:

Real-time X-ray scattering study of perovskite annealing by infrared irradiation.

5th International Conference on Perovskite Solar Cells and Optoelectronics (PSCO19). Lausanne, Switzerland. 30 Sep – 2 Oct 2019

Bibliography

1. Kojima, A., Teshima, K., Shirai, Y. & Miyasaka, T. Organometal halide perovskites as visible-light sensitizers for photovoltaic cells. *J. Am. Chem. Soc.* **131**, 6050–6051 (2009).
2. Yang, W. S. *et al.* Iodide management in formamidinium-lead-halide-based perovskite layers for efficient solar cells. *Science (80-.).* **356**, 1376–1379 (2017).
3. Green, M. A., Ho-Baillie, A. & Snaith, H. J. The emergence of perovskite solar cells. *Nat. Photonics* **8**, 506–514 (2014).
4. NREL. Best Research-Cell Efficiency Chart. Photovoltaic Research. Accessed Nov. 2021. https://www.nrel.gov/pv/cell-efficiency.html (2021).
5. Kim, M. *et al.* Conformal quantum dot–SnO 2 layers as electron transporters for efficient perovskite solar cells. *Science (80-.).* **375**, 302–306 (2022).
6. Wang, R. *et al.* A Review of Perovskites Solar Cell Stability. *Adv. Funct. Mater.* **29**, (2019).
7. Smith, I. C., Hoke, E. T., Solis-Ibarra, D., McGehee, M. D. & Karunadasa, H. I. A Layered Hybrid Perovskite Solar-Cell Absorber with Enhanced Moisture Stability. *Angew. Chemie Int. Ed.* **53**, 11232–11235 (2014).
8. Ghimire, S. & Klinke, C. Two-dimensional halide perovskites: synthesis, optoelectronic properties, stability, and applications. *Nanoscale* **13**, 12394–12422 (2021).
9. Ling, X. *et al.* 14.1% CsPbI3 Perovskite Quantum Dot Solar Cells via Cesium Cation Passivation. *Adv. Energy Mater.* **9**, 1–9 (2019).
10. Protesescu, L. *et al.* Nanocrystals of Cesium Lead Halide Perovskites (CsPbX3, X = Cl, Br, and I): Novel Optoelectronic Materials Showing Bright Emission with Wide Color Gamut. *Nano Lett.* **15**, 3692–3696 (2015).
11. Wang, Y. *et al.* All-Inorganic Quantum-Dot LEDs Based on a Phase-Stabilized α-CsPbI 3 Perovskite. *Angew. Chemie Int. Ed.* **60**, 16164–16170 (2021).
12. Zhang, X., Wang, Q., Jin, Z., Zhang, J. & Liu, S. (Frank). Stable ultra-fast broad-bandwidth photodetectors based on α-CsPbI 3 perovskite and NaYF 4 :Yb,Er quantum dots. *Nanoscale* **9**, 6278–6285 (2017).
13. Sanchez, S., Hua, X., Phung, N., Steiner, U. & Abate, A. Flash Infrared Annealing for Antisolvent-Free Highly Efficient Perovskite Solar Cells. *Adv. Energy Mater.* **8**, (2018).
14. Bai, S. *et al.* Planar perovskite solar cells with long-term stability using ionic liquid additives. *Nature* vol. 571 245–250 (2019).

15. Kim, M. *et al.* Methylammonium Chloride Induces Intermediate Phase Stabilization for Efficient Perovskite Solar Cells. *Joule* **3**, 2179–2192 (2019).
16. Sahayaraj, S. *et al.* Combination of a large cation and coordinating additive improves carrier transport properties in quasi-2D perovskite solar cells. *J. Mater. Chem. A* **9**, 9175–9190 (2021).
17. Liu, Z. *et al.* Controllable Two-dimensional Perovskite Crystallization via Water Additive for High-performance Solar Cells. *Nanoscale Res. Lett.* **15**, 108 (2020).
18. Yang, J. *et al.* A review on improving the quality of Perovskite Films in Perovskite Solar Cells via the weak forces induced by additives. *Applied Sciences (Switzerland)* vol. 9 (2019).
19. Xue, Y., Yuan, J., Liu, J. & Li, S. Controllable Synthesis of 2D Perovskite on Different Substrates and Its Application as Photodetector. *Nanomaterials* **8**, 591 (2018).
20. Pant, N., Yanagida, M., Shirai, Y. & Miyano, K. Substrate dependent morphological and electronic properties of lead halide perovskite solar cells. in *Proceedings of the 2nd Asia-Pacific Hybrid and Organic Photovoltaics* (Fundació Scito, 2017). doi:10.29363/nanoge.ap-hopv.2018.026.
21. Sun, S. *et al.* 0D Perovskites: Unique Properties, Synthesis, and Their Applications. *Adv. Sci.* **8**, 2102689 (2021).
22. Swarnkar, A. *et al.* Quantum dot–induced phase stabilization of α-CsPbI 3 perovskite for high-efficiency photovoltaics. *Science (80-.).* **354**, 92–95 (2016).
23. Hao, M. *et al.* Ligand-assisted cation-exchange engineering for high-efficiency colloidal Cs1−xFAxPbI3 quantum dot solar cells with reduced phase segregation. *Nat. Energy* **5**, 79–88 (2020).
24. Wheeler, L. M. *et al.* Targeted Ligand-Exchange Chemistry on Cesium Lead Halide Perovskite Quantum Dots for High-Efficiency Photovoltaics. *J. Am. Chem. Soc.* **140**, 10504–10513 (2018).
25. Sahoo, S. K., Manoharan, B. & Sivakumar, N. Introduction. in *Perovskite Photovoltaics* 1–24 (Elsevier, 2018). doi:10.1016/B978-0-12-812915-9.00001-0.
26. Cui, J. *et al.* Recent progress in efficient hybrid lead halide perovskite solar cells. *Sci. Technol. Adv. Mater.* **16**, (2015).
27. Bartel, C. J. *et al.* New tolerance factor to predict the stability of perovskite oxides and halides. *Sci. Adv.* **5**, 1–10 (2019).
28. Huang, F., Li, M., Siffalovic, P., Cao, G. & Tian, J. From scalable solution fabrication of perovskite films towards commercialization of solar cells. *Energy Environ. Sci.* **12**,

518–549 (2019).

29. Park, N. G. Perovskite solar cells: An emerging photovoltaic technology. *Materials Today* vol. 18 65–72 (2015).
30. Jena, A. K., Kulkarni, A. & Miyasaka, T. Halide Perovskite Photovoltaics: Background, Status, and Future Prospects. *Chem. Rev.* **119**, 3036–3103 (2019).
31. Yin, W.-J., Yang, J.-H., Kang, J., Yan, Y. & Wei, S.-H. Halide Perovskite Materials for Solar Cells: A Theoretical Review. *J. Mater. Chem. A* **3**, 10715–10722 (2014).
32. Li, W. *et al.* Hybrid Perovskites ; New Opportunities beyond Oxides. 1–47.
33. Moore, D. T. *et al.* Crystallization kinetics of organic-inorganic trihalide perovskites and the role of the lead anion in crystal growth. *J. Am. Chem. Soc.* **137**, 2350–2358 (2015).
34. Köster, U. Crystallization of amorphous silicon films. *Phys. Status Solidi* **48**, 313–321 (1978).
35. Saidaminov, M. I., Mohammed, O. F. & Bakr, O. M. Low-Dimensional-Networked Metal Halide Perovskites: The Next Big Thing. *ACS Energy Lett.* **2**, 889–896 (2017).
36. Grancini, G. & Nazeeruddin, M. K. Dimensional tailoring of hybrid perovskites for photovoltaics. *Nature Reviews Materials* vol. 4 4–22 (2019).
37. Kim, J. *et al.* Alkali acetate-assisted enhanced electronic coupling in CsPbI3 perovskite quantum dot solids for improved photovoltaics. *Nano Energy* **66**, 104130 (2019).